Electron count dictates phase separation in Heusler alloys

Justin A. Mayer [1,*] and Ram Seshadri [1,2]

[1]*Materials Department and Materials Research Laboratory, University of California, Santa Barbara, California 93106, USA*

[2]*Department of Chemistry and Biochemistry, University of California, Santa Barbara, California 93106, USA*

(Received 8 September 2021; revised 1 March 2022; accepted 5 April 2022; published 12 May 2022)

Phase separation—and conversely, the propensity for solid-solution formation—in half-Heusler (XYZ) and Heusler (XY_2Z) compounds is suggested from first-principles electronic-structure-based modeling to be strongly linked to the electronic behavior of the end-members. Alloying between distinct pairs of half-Heusler and Heusler compounds is possible at accessible processing temperatures when the two end-members are either isoelectronic or metallic. The formation of a band gap in semiconducting half-Heusler compounds is associated with significant stabilization. Attempts to create solid solutions with a semiconducting half-Heusler compound would lead to phase separation across the tie line because of the energy penalty associated with filling states in the gap. The alloying between two Heusler compounds, however, is expected even when the electronic behaviors of the end-members differ—clearly demonstrating the distinction between the underlying bonding within half-Heuslers and Heuslers: Half-Heuslers are well-defined intermetallics, whereas Heuslers tend to behave in a manner more in line with conventional alloys. The simple proxy related to electronic structure developed here differentiates Heusler and half-Heusler compositions that truly alloy from those that phase separate, aiding in the pursuit of reliable first-principles materials discovery.

DOI: 10.1103/PhysRevMaterials.6.054406

I. INTRODUCTION

In 1903 Heusler reported his finding of ferromagnetism within alloys of composition close to, or equal to, $MnCu_2Al$ [1]. This observation was entirely unexpected at the time as ferromagnetism was associated solely with Fe, Co, and Ni and their compounds. The phenomenon of antiferromagnetism (pertinent for Mn) was not known until the seminal work of Néel a few decades later [2]. Since the original report by Heusler, ordered compounds with the chemical formula XY_2Z or XYZ, and crystal structure $L2_1$ or $C1_b$, have become known as Heusler compounds and half-Heusler compounds, respectively. Their crystal structures are shown for reference in Fig. 1.

A note on nomenclature is appropriate here. The description XY_2Z is preferred over X_2YZ in describing Heusler compounds for several reasons. There is the obvious relation between the XYZ half-Heusler and the XY_2Z Heusler, viz., that XZ describes a rocksalt structure in both. Following the usual rules of chemical nomenclature, the order of the electronegativities χ is usually $\chi_X < \chi_Y < \chi_Z$, which also justifies Y after X. A third reason is crystallographic. The XYZ half-Heusler derives from the Heusler XY_2Z without any change in internal atomic positions simply through application of the group-subgroup relation between $Fm\bar{3}m$ and $F\bar{4}3m$.

Half-Heusler and Heusler materials have been prepared from a wide variety of elements where, in general, the X site and Y site correspond to an earlier and later transition metal, and the Z site is occupied by a main group element. The exceptional properties of these compounds derive from their broadly varying material properties that are readily controlled via valence electron count—a fact that has been extensively outlined in the review by Graf *et al.* [3] This has prompted a great deal of academic interest within this class of compounds as researchers aspire to leverage chemical doping on one of the Heusler or half-Heusler sublattices to realize multifunctional materials such as topological superconductors [4], or tune the location of Weyl nodes [5]. Despite the innate power of these rules for predicting material properties, the feasibility of capturing the predicted properties through a chemically doped solid solution is often willfully overlooked.

Studies pertaining to the solid solubility between two half-Heuslers, two Heuslers, or a half-Heusler and a Heusler from first principles have advanced parallel to other areas of Heusler research, particularly with the intention of identifying novel nanostructured semiconducting Heuslers or half-Heuslers that exhibit enhanced thermoelectric efficiency [6–9]. Kocevski and Wolverton [8] sought to identify all potential two-phase systems that include either a semiconducting Heusler or half-Heusler matrix and an additional Heusler or half-Heusler that could act as a precipitate phase. In total, their work identified 31 potential pairings—each of which was either isoelectronic or differed by only ± 1 in valence electron count—and had a lattice mismatch of less than 3%. This work laid the foundation to consider the energetics of alloy formation within the family of Heuslers and half-Heuslers and prompts the following questions: (i) Can valence electron count and lattice mismatch be used to unambiguously establish the tendency for two ordered compounds within the family of Heuslers and half-Heuslers to alloy? (ii) Is there a clear understanding regarding why certain Heusler and or half-Heusler pairs fall below or above a reasonably defined

*Corresponding author: jmayer@mrl.ucsb.edu

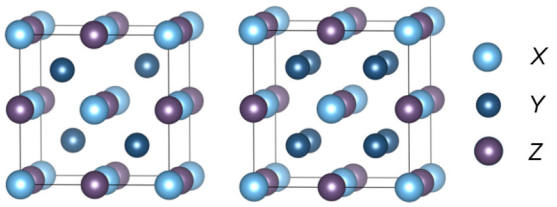

FIG. 1. Left: The half-Heusler crystal structure, which consists of three interpenetrating face-centered cubic lattices, each of which is occupied by one of the three constituent elements within its chemical formula XYZ. The point group of this crystal is T_d, and the space group is $F\bar{4}3m$. Right: The Heusler crystal structure, which consists of four interpenetrating face-centered cubic lattices. The fourth sublattice, which is unoccupied in the half-Heusler, is occupied by a second Y atom to yield a chemical formula XY_2Z. The point group of this crystal is O_h, and the space group is $Fm\bar{3}m$.

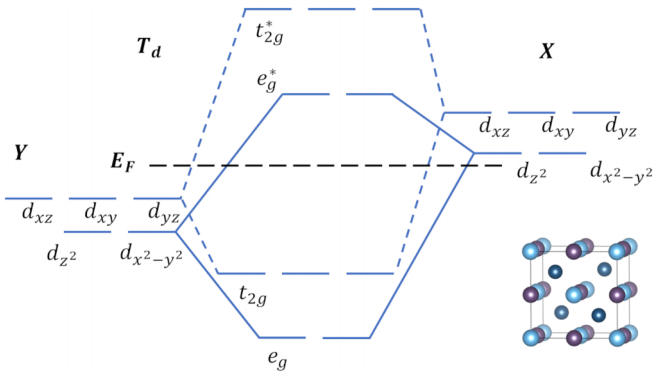

FIG. 2. Schematic of d-d-orbital hybridization between the X element and the Y element within a half-Heusler of chemical formula XYZ. Both the X element and Y element experience tetrahedral crystal field splitting due to the $C1_b$ crystal structure. These orbitals then hybridize according to the irreducible representations of the T_d point group. The electronegativity between the X element and the Y element dictates the size of the band gap.

immiscibility criterion? In answering these questions, an understanding of the bonding mechanisms in both Heuslers and half-Heuslers is crucial since it is these mechanisms that may eventually lead to instabilities in electronic structure upon alloying.

An understanding of the electronic structure of these ordered compounds almost certainly begins with the well-known first-principles prediction of half-metallic ferromagnetism within the half-Heusler MnNiSb by de Groot *et al.* [10]. This work was then followed by the unexpected experimental discovery of semiconducting behavior in half-Heuslers of the form MNiSn (where M = Ti, Zr, Hf) by Aliev *et al.* [11] and ultimately led to Öğüt and Rabe [12] completing a thorough set of first-principles calculations on MNiSn and MNi$_2$Sn, highlighting that the half-Heusler compounds are particularly stable due to the opening of a band gap which only exists if the elements M and Sn form the rocksalt sublattice of the $C1_b$ crystal structure. Nanda and Dasgupta [13] and Galanakis *et al.* [14] then unequivocally identified the nature of the band gap present within the half-Heusler (whether the half-Heusler of interest is semiconducting or half-metallic). Kandpal *et al.* [15] presented the link between bonding patterns in 8- and 18-electron half-Heusler compounds and suggested that half-Heuslers are best seen as stuffed, covalently bonded zinc blendes in analogy with the Zintl rules for intermetallics.

The simplest depiction of the bonding based on some of the aforementioned work is as follows: The d orbitals of the X and Y transition metals hybridize to form five bonding and five antibonding orbitals, while the main group Z element contributes one s orbital and three p orbitals low lying in energy. The d-d hybridization between the X and Y transition metals therefore produces the band gap observed in semiconducting half-Heuslers, as shown schematically in Fig. 2. The concept of "valence precision" can be inferred from this bonding model since any half-Heusler with 18 electrons (nine in each spin channel) will be semiconducting. Half-Heuslers with greater than 18 valence electrons, if stable, will then be a half-metallic ferromagnet, as any additional electrons populate the majority spin channel, preserving the band gap in the minority spin channel. The net magnetization M of any half-Heusler therefore follows a Slater-Pauling curve [14] dictated by the total number of valence electrons N_v, where $M = N_v - 18$.

Similarly, some ordered Heusler compounds have been found to be semiconducting [16], and a number of Mn-containing Heuslers have been predicted to be half-metallic ferromagnets [17,18]. It is clear that the nature of the band gaps within Heuslers (point group O_h) will differ slightly from their half-Heusler counterparts (point group T_d) and therefore require a different bonding mechanism to describe their electronic properties. This prompted Galanakis *et al.* to provide a detailed analysis of the bonding present within MnY_2Z Heuslers based on Y = Co, Fe, Ru, and Rh [19]. Specifically, Galanakis *et al.* argue that it is best to assess the bonding present within Heuslers by first considering Y-Y d-orbital hybridization which, in theory, leads to the formation of five bonding orbitals, three of which transform according to the T_{2g} irreducible representation of O_h and two of which transform according to the E_g irreducible representation of O_h, and five antibonding orbitals, three of which transform according to the T_{1u} irreducible representation and two of which transform according to the E_u irreducible representation. The resulting Y-Y d-orbital hybridization is shown schematically in Fig. 3. Similar to the half-Heusler, these orbitals will then hybridize further with the X element, but the underlying O_h symmetry prohibits the d orbitals of the X element from hybridizing with the t_{1u} or e_u electronic states formed via Y-Y hybridization. The final electronic structure therefore includes—in addition to the t_{1u} and e_u orbitals—three bonding and antibonding orbitals that transform according to the T_{2g} irreducible representation and two bonding and antibonding orbitals that transform according to the E_g irreducible representation. This ultimately leads to a final electronic structure in line with the diagram shown in Fig. 3. Galanakis *et al.* therefore assert that the band gap observed in Heuslers is formed by the slight splitting between the t_{1u} orbitals and the e_u orbitals, which are expected to lie above and below the Fermi level, respectively. Including the low-lying s and three p orbitals from the Z element, a semiconducting Heusler therefore reflects

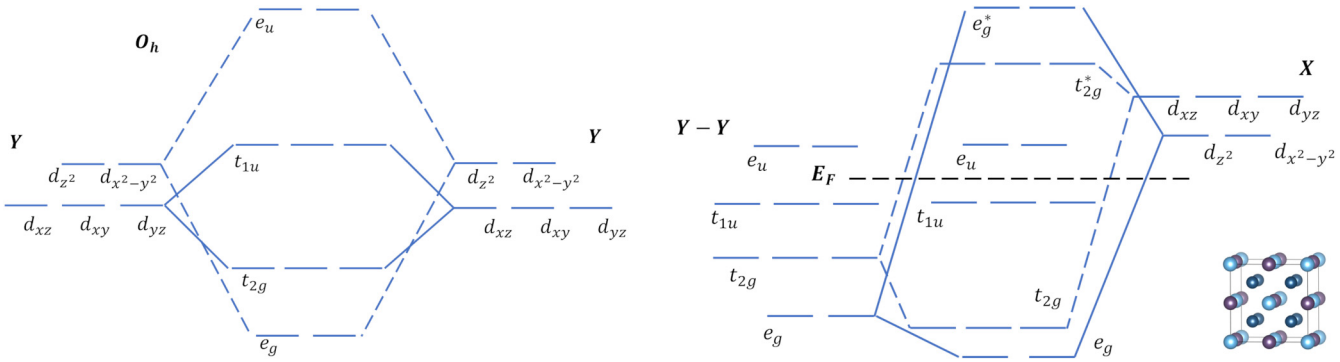

FIG. 3. Schematic of d-d-orbital hybridization between both Y elements as well as X and Y elements in Heuslers with chemical formula XY_2Z. Left: The model assumes that the d orbitals of the two distinct Y atoms, which are octahedrally coordinated with one another, hybridize first. Right: The resulting orbitals can then hybridize with the tetrahedrally coordinated X atom of the $L2_1$ crystal structure. d-orbital hybridization between the X atom and the Y-Y sublattice is dictated by the O_h point group, which leads to a narrow band gap caused by the e_u and t_{1u} orbitals of the Y-Y sublattice that cannot further hybridize with the X atom.

a valence precision of 24 valence electrons (as opposed to the 18 valence electron semiconducting half-Heuslers), while the net magnetization of half-metallic ferromagnetic Heuslers follows a Slater-Pauling curve of the form $M = N_v - 24$ [19].

The bonding mechanisms outlined above provide a great deal of insight regarding half-Heusler and Heusler stability. In particular, the fact that the band gap of a half-Heusler is caused by X-Y d-orbital hybridization means that this band gap is often much larger than the band gap caused by Y-Y d-orbital hybridization of a Heusler. This implies that there is a large energy cost that accompanies the disruption of the half-Heusler band gap. However, it is less clear how significant the smaller Heusler band gap is in stabilizing the Heusler structure. Herein we aim to establish a reasonable first-principles proxy for evaluating the extent to which alloying upon either a Heusler or a half-Heusler sublattice disturbs the electronic structure of the ordered end-members. The energetics of this alloying process, which we assess via the first-principles approach outlined by Kocevski and Wolverton [8], allows us to assess the solid solubility of an element within a host Heusler or half-Heusler lattice, such that the materials community can easily identify elements and host lattices that are amenable to chemical doping. We also provide the minimum processing temperatures required to stabilize a solid solution of candidate Heusler and/or half-Heusler alloys of interest.

An interesting point regarding the phase-separating systems discussed is that all of them violate the simple Hume-Rothery rules of alloy formation, since the end-member structures are the same, the size changes are minor, etc. However, Hume-Rothery himself was no stranger to the role that electron counting and electronic structure play in determining alloy formation, and one could potentially see the work reported here as being inspired by his original ideas [20,21].

II. METHODS

Since this work aims to aid experimentalists in identifying relevant Heusler or half-Heusler material systems for further alloying, the majority of all atomistic calculations are performed on Heusler and half-Heusler compounds that have been previously determined to lie on the convex hull of their respective ternary phase diagrams. These material systems were identified with the help of the Open Quantum Materials Database (OQMD) [22,23]. In particular, using the PYTHON application programming interface (API) wrapper qmpy_rester [24], all Heusler and half-Heusler compounds cataloged by the OQMD were enumerated and sorted by valence electron count and stability (where stability is a simple binary variable: "yes" if the system is on the convex hull or "no" if the system is not). Candidate systems were derived from the resulting list of compounds when both were stable and shared two common elements. Based on this process, the majority of the candidate alloys within this contribution exist along experimentally relevant tie lines, meaning that the alloys studied here exist between two end-members that have been deemed to be stable at $T = 0$ K. There are, however, three additional candidate alloy systems included because of the preexisting experimental work on them. These are $Mn_{1-x}Ti_xCoSb$, $TiNi_{1+x}Sn$, and $NbCo_{1+x}Sn$. While MnCoSb, $TiNi_2Sn$, and $NbCo_2Sn$ do not lie on their respective convex hulls, the additional end-member of these candidate alloy systems does. This fact, along with the experimental work that exists on $Mn_{1-x}Ti_xCoSb$ [25], $TiNi_{1+x}Sn$ [26,27], and $NbCo_{1+x}Sn$ [28,29], provided enough motivation to include them within this study. For systems where the energy of mixing for a candidate alloy is negative, this system is more stable than the end-members at $T = 0$ K and suggests the existence of a quaternary intermetallic or of a disordered alloy (depending on the magnitude of the energy of mixing). However, when the energy of mixing is positive, the candidate alloy requires entropic degrees of freedom to be stabilized, and the potential for experimentally realizing a single phase will be dictated by the temperature at which entropic degrees of freedom overtake the energy of mixing.

The solubility within any given candidate alloy can be determined based on a rather simple model for the solvus lines which has been discussed in detail by Kocevski and Wolverton [8]. In brief, this approach assumes that the energy of mixing at absolute zero temperature of a solute alloying on a particular sublattice of a host crystal can be used to predict the equilibrium solvus line at elevated temperatures

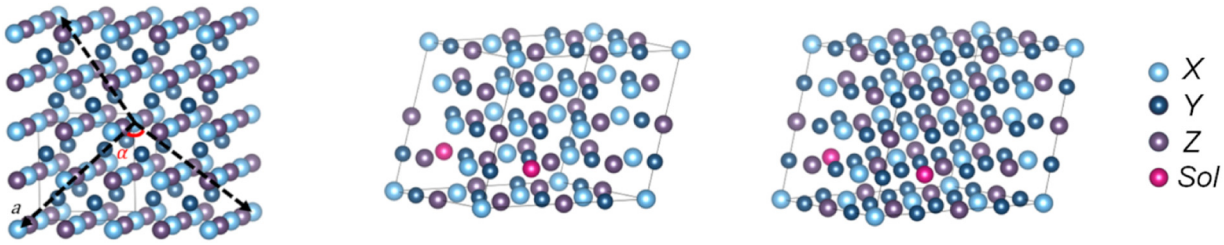

FIG. 4. Left: The relationship between the conventional unit cell of the half-Heusler and the supercell used to calculate the energy of formations of candidate alloys. The lattice vectors of the supercell lie along the [111] directions of the conventional unit cell, are of length a, and make an angle $\alpha = 109.5^\circ$ with one another. Center: A representative solute supercell for X-site substitution within a half-Heusler. Right: A representative solute supercell for X-site substitution within a Heusler.

via Eq. (1).

$$x_s(T) \approx \exp\left(-\frac{\Delta E_f}{k_B T}\right), \tag{1}$$

where ΔE_f is the $T = 0$ K internal energy of mixing for the solute within the dilute limit calculated via density functional theory (DFT) and k_B is the Boltzmann constant. Clearly, there are several approximations that yield this expression for the solvus line, but this rather crude approximation proves to be a reliable proxy when the internal energy of mixing of the solute atom is very large and dominates the expression for the free energy of mixing. When this assumption holds, a supercell large enough to avoid fictitious solute-solute interactions caused by the periodic boundary conditions of DFT can be used to approximate the equilibrium solvus lines at elevated temperatures. As discussed by Kocevski and Wolverton, a 48-atom (64-atom) supercell (a cell four times as large as the conventional fcc unit cell and 16 times larger than the primitive fcc cell) is more than ample for this type of calculation when considering the formation of a defect within a half-Heusler (Heusler). Since the crystal structures of a Heusler and half-Heusler contain three possible alloying sites, X-site substitutions, Y-site substitutions, and Z-site substitutions, all three types of alloys are considered in this paper. As an example, the internal energy of mixing for a solute atom, A, on the X site within a host half-Heusler lattice with chemical formula XYZ is then given by Eq. (2).

$$\Delta E_f = E_{X(A)YZ} - \frac{N_X E_{XYZ} - N_A E_{AYZ}}{N_S}, \tag{2}$$

where N_X and N_A are the number of X and A atoms on the X site, respectively, and N_S is the total number of X sites within the 48-atom half-Heusler supercell. $E_{X(A)YZ}$, E_{XYZ}, and E_{AYZ} are the DFT formation energies of the defect structure, XYZ end-member, and AYZ end-member, respectively. Each of these energies is calculated based on the supercell structure to avoid computational errors that might arise if the energetics of the XYZ and AYZ end-members were calculated using the primitive unit cells. The 48-atom supercell in relation to the conventional cubic half-Heusler cell is shown within Fig. 4. Additionally, an example of a supercell used to calculate the energy of formation of a defect for X–site substitution is also shown for the half-Heusler and Heusler in Fig. 4. The Heusler X-site alloy has an additional 16 atoms that populate the vacant face-centered-cubic lattice of the half-Heusler crystal.

All calculations were implemented within the Vienna *ab initio* simulation package (VASP) [30] using projector-augmented-wave (PAW) pseudopotentials [31,32] within the Perdew-Burke-Ernzerhof (PBE) generalized gradient approximation (GGA) [33]. A plane-wave energy cutoff of 550 eV was used, and spin polarization was also included. A Monkhorst-Pack [34] mesh of $7 \times 7 \times 7$ k points was used for all solute supercell calculations. The cells were initially allowed to relax, with the unit cell shape, unit cell volume, and ion positions permitted to vary. A final static calculation was then performed using the tetrahedron method to determine the formation energy of each supercell. An energy convergence criterion of 10^{-6} was used, and the magnetic moments of transition metal elements were initialized with magnetic moments of 4 μ_B, whereas Mg, Sc, Y, and main group elements were initialized with magnetic moments of 1 μ_B.

Once the energetics of all candidate alloys were calculated, additional calculations were performed on a select group of material systems to explore the influence of electronic structure on miscibility. To compare the electronic structure of supercells that include a solute atom with the electronic structure of the end-members, the band dispersion of the Brillouin zone of the supercell is unfolded into the Brillouin zone of the primitive cell. Unfolding is performed via the unfolding algorithm outlined by Popescu and Zunger [35] made available in the PYTHON class VASPBANDUNFOLDING [36]. The resulting band diagram is plotted based on the spectral weight $P_{\vec{K}m}$ calculated by projecting each supercell plane-wave state $|\vec{K}m\rangle$ into all primitive Brillouin zone plane-wave states with wave vector $\vec{k}_j$ as

$$P_{\vec{K}m}(\vec{k}_j) = \sum_n |\langle \vec{K}m | \vec{k}_j n \rangle|^2, \tag{3}$$

where the indices m and n reflect the mth and nth bands of the supercell and primitive cell wave function, respectively. Since the two Brillouin zones are related to one another by a user-determined transformation matrix, all information required to determine the spectral weight is contained within the plane-wave coefficients of the relaxed supercell (as discussed in Ref. [35]).

Lastly, the impact of electron correlation on the predicted solubility of several candidate alloy systems was investigated via Dudarev *et al.*'s $U - J = U_{\text{eff}}$ formalism [37] implemented within GGA + U calculations. The purpose of these additional calculations was to qualitatively assess whether the

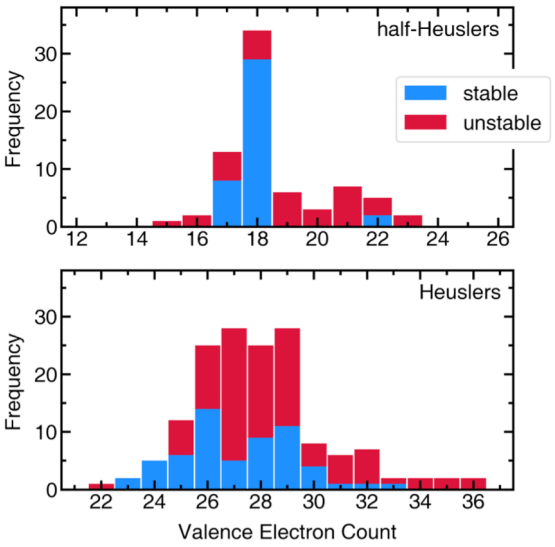

FIG. 5. Frequency of half-Heuslers and Heuslers within the Open Quantum Materials Database that either lie on the convex hull of their respective ternary phase diagram and are therefore stable, or are otherwise unstable. The frequency is plotted against the valence electron count of each half-Heusler or Heusler. Almost all stable half-Heuslers are valence precise with 18 valence electrons, whereas the stable Heuslers do not necessarily require the valence precision of 24 valence electrons.

location and shape of the electronic states introduced by a solute atom are significantly altered by the electron correlations that are certainly present in compounds containing 3*d* transition metals—particularly Heusler compounds with narrow energy bands. We follow the procedure previously applied to transition-metal-based Heusler compounds outlined by Kandpal *et al.* [38] wherein the U_{eff} parameter for each 3*d* transition metal included within a candidate alloy system is set to 0, 5, and 10% of its atomic Coulomb exchange parameter. The energetics for each U_{eff} parameter is then therefore referred to as U_{00}, U_{05}, and U_{10}, respectively.

III. ENUMERATED CANDIDATE ALLOY SYSTEMS

The frequency of Heusler and half-Heusler end-members that are identified as either stable or unstable within the OQMD is plotted as a function of valence electron count in Fig. 5. Interestingly, valence-precise half-Heuslers are overwhelmingly stable in comparison to their metallic counterparts. The family of Heuslers, however, do not appear to require valence precision (24 valence electrons) to lie on the convex hull of their respective $T = 0$ K ternary phase space. Instead, the Heusler crystal structure can accommodate compounds with an assortment of valence electron counts—leading to numerous stable Heusler metals. This fact may very well reflect the unique bonding of the half-Heusler crystal structure discussed above. The large band gap created by *X*-*Y* hybridization of the half-Heusler crystal structure promotes the formation of almost exclusively 18-valence-electron half-Heuslers—a phenomenon that has been discussed previously by Anand *et al.* [39] in relation to the stability of 19-valence-electron half-Heuslers. It was found that 19-valence-electron half-Heuslers that have been successfully prepared are most likely stabilized by vacancies on the *X*-site sublattice that ultimately ensure valence precision and the preservation of a large band gap.

It is natural to expect that alloying trends within the family of half-Heuslers and Heuslers will follow a similar dependence on valence electron count. For this reason, the resulting number of valence electrons of an alloy created from two end-members identified in Fig. 5 is separated into distinct classes. For the half-Heusler alloys, three classes are used: electron-deficient, isoelectronic, and electron-rich alloys. Electron-deficient and electron-rich alloys refer to alloys that have either fewer than 18 electrons or more than 18 electrons, respectively, whereas isoelectronic alloys encompass all alloys that do not experience a change in electron count upon alloying.

For the Heusler alloys, four distinct classes are used: electron-deficient, isoelectronic, electron-rich, and metallic. The first three classes are essentially identical to the half-Heusler case except that the number of electrons used to separate electron-deficient and electron-rich alloys is 24 instead of 18. Again, referring to Fig. 5, the number of 24-electron Heuslers that are stable at $T = 0$ K is significantly lower than the number of stable 18-electron half-Heuslers. Isoelectronic Heusler alloys are therefore much more likely to be composed of two alloys that have more than 24 electrons. The fourth classifier, termed "metallic," then encompasses all alloying candidates that possess more than 24 electrons but consist of two end-members with differing electron count.

When establishing trends related to the energy of formation within the family of Heuslers and half-Heuslers, the lattice misfit $|\delta|$ is an additional descriptor that can be used in tandem with valence electron count. This will aid in the disentanglement of structural contributions to the energy of formation (caused by lattice misfit) from electronic contributions to the energy of formation (caused by electron count). Since all Heuslers and half-Heuslers are cubic, the lattice misfit is calculated as the relative percentage difference between the lattice parameters of the end-members of a candidate alloy via Eq. (4):

$$|\delta| = (|a_{XYZ} - a_{AYZ}|)/a_{XYZ} \times 100\%. \tag{4}$$

IV. THE ENERGETICS OF CANDIDATE ALLOY SYSTEMS

As discussed in Methods, the solvus line approximation outlined by Kocevski and Wolverton [8] breaks down at high concentration and for low energies of formation. This can be seen in Fig. 6 as a ΔE_f of 0.10 or 0.05 eV leads to a clear change in concavity of the solvus line at a composition close to $x = 0.1$. This, of course, is not consistent with the behavior of experimental solvus lines of alloys with low energies of formation. Instead, entropic degrees of freedom stabilize the solid solution across the entire tie line, as depicted schematically in Fig. 6. Therefore, to place an upper bound on the energy of formation at which entropic degrees of freedom can overcome the energy penalty associated with solute-solute interactions across the entire tie line, we consider the thermodynamic model that Eq. (1) is derived from—specifically, the

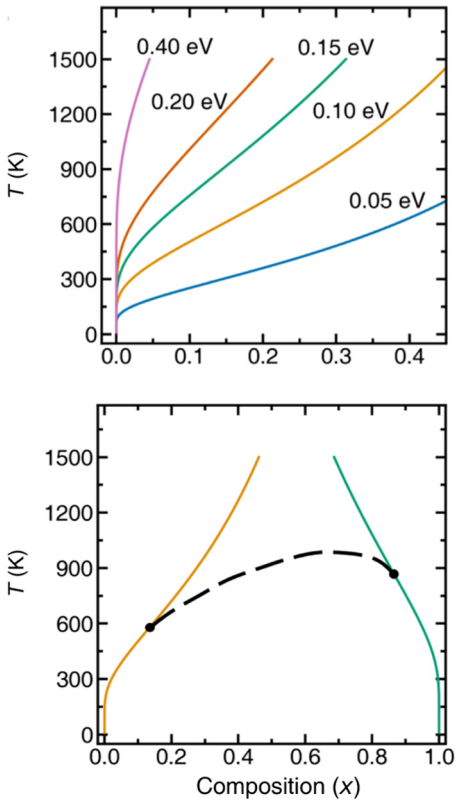

FIG. 6. Top: The behavior of Eq. (1) for different values of ΔE_f. For low values of ΔE_f the solvus line dramatically breaks down at intermediate compositions. This is because Eq. (1) has an inflection point whereas real solvus lines do not. Bottom: A model phase diagram across the tie line of two end-members. If an alloy between two half-Heuslers with chemical formula $X_{1-x}A_xYZ$ is considered, for example, then the ΔE_f of incorporating an A solute atom will, in general, differ from the ΔE_f of incorporating an X solute atom. Here, it is assumed that these two ΔE_f values are 0.10 and 0.15 eV, respectively. The inflection points of each solvus line are marked by black circles, and the dashed line connecting the two inflection points schematically depicts the anticipated behavior of the "true" solvus line at intermediate compositions.

regular model for the free energy ΔG_f of a solid solution:

$$\Delta G_f = x(1-x)\Delta E_f + k_B T[x\ln(x) + (1-x)\ln(1-x)]. \tag{5}$$

Within this model, the solid solution is the most unstable, for any ΔE_f and T, at a composition of $x = 0.5$. A solid solution is therefore stable across the entire tie line at the temperature, $T_{\text{min}}^{\text{SS}}$, where $\Delta G_f = 0, x = 0.5$. This leads to the following expression for $T_{\text{min}}^{\text{SS}}$:

$$T_{\text{min}}^{\text{SS}} = \Delta E_f / 4k_B \ln(2). \tag{6}$$

If we assume that $T_{\text{min}}^{\text{SS}}$ is a reasonable approximation for the temperature at which a solid solution should be expected to exist across the entire tie line, then one can identify 0.28 eV as the energy of formation where $T_{\text{min}}^{\text{SS}}$ corresponds to the fairly standard annealing temperature of 900 °C. Based on this thought process, we believe that an energy of formation of 0.28 eV is a qualitatively reasonable upper bound for the ΔE_f of an alloy in which a solid solution is expected to exist across the entire tie line. This qualitative upper bound allows for the ΔE_f's reported in this paper to be interpreted in the following way: (i) If the ΔE_f of the candidate alloy falls above the upper bound, the system phase separates and Eq. (1) provides a rather reliable prediction for the expected composition of the dilute alloy that would be present within the experimental microstructure at a given processing temperature. (ii) If the ΔE_f of the candidate alloy falls below the upper bound, Eq. (6) provides a processing temperature that is expected to stabilize a solid solution across the entire tie line.

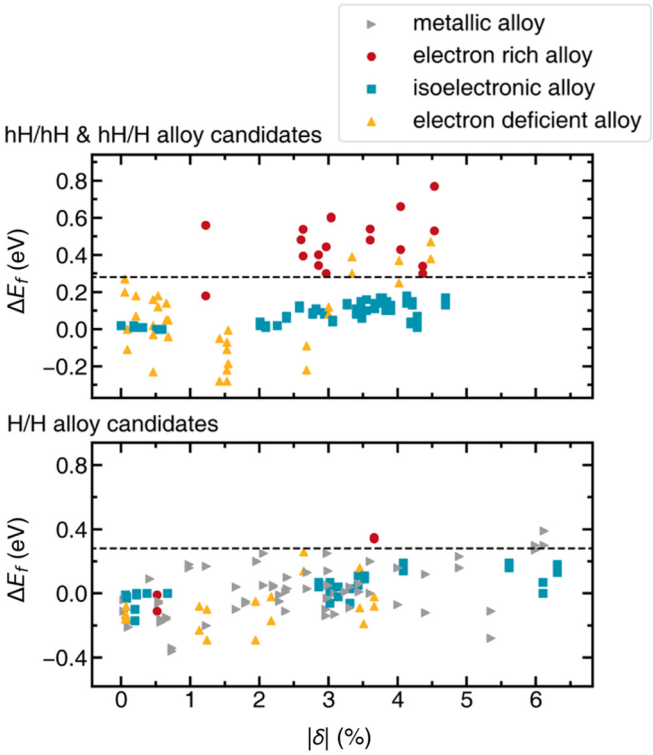

FIG. 7. Top: The energy of formation ΔE_f plotted against lattice misfit $|\delta|$ for all half-Heusler (hH/hH) alloy candidates studied. The half-Heusler/Heusler (hH/H) alloy systems are also included here as they can be thought of as the incorporation of Y atoms of a half-Heusler with chemical formula XYZ onto the additional vacant Y sublattice. Bottom: The energy of formation ΔE_f plotted against lattice misfit $|\delta|$ for all Heusler (H/H) alloy candidates studied. The dashed line corresponds to the qualitative upper bound for the ΔE_f ($\Delta E_f = 0.28$ eV) of an alloy in which a solid solution is expected to exist across the entire tie line.

A. Response of half-Heusler systems to alloying

It is now possible to reconcile the general alloying behavior of both the half-Heusler candidate alloys and the Heusler candidate alloys. Beginning with the half-Heuslers, Fig. 7 shows that there is a remarkable difference between the isoelectronic alloy systems and the electron-rich alloy systems. In general, the isoelectronic alloys remain below the 0.28 eV energy of formation threshold, suggesting that they can be stabilized as solid solutions across the entire tie line. It is also noteworthy that as lattice misfit is increased, there is only a slight increase in the energy of formation for isoelectronic alloy candidates.

Isoelectronic half-Heusler alloys with a lattice misfit less than or equal to 5% can therefore be expected to remain miscible in one another, albeit with processing temperatures of approximately 800 or 900 °C for lattice misfits on the order of 4 or 5%, respectively. However, the electron-rich alloys exhibit minimal solubility across the same range of lattice misfits. Clearly, the change in electron concentration is the main driving force for phase separation in half-Heusler alloying candidates. All alloying candidates studied within this contribution are summarized in the Appendix in Tables II, III, and IV, which tabulate X-site, Y-site, and Z-site substitutions, respectively.

The stark contrast in the alloying behavior of model systems $Mn_{1-x}Ti_xCoSb$ and $Zr_{1-x}Ti_xCoSb$ is a particularly strong example of the role the electronic contribution of the solute atom can play in driving phase separation within the family of half-Heusler/half-Heusler alloys. In particular, $Mn_{1-x}Ti_xCoSb$ provides a unique opportunity to explore the impact of electronic structure on the miscibility between two intermetallic end-members that share the same host lattice because of its minimal lattice misfit of $|\delta| = 1.22\%$. As seen from Fig. 7, a lattice misfit of this magnitude within an *isoelectronic* alloy produces a negligible contribution to the total energy of formation. The large, asymmetric energy of formation observed within the candidate alloy system $Mn_{1-x}Ti_xCoSb$ can therefore be assumed to be a direct result of the electronic disparity between the end-members TiCoSb and MnCoSb. Figure 8 clearly illustrates this fact based on the dispersion and location of the defect states present within the representative superstructures of Ti-rich and Mn-rich $Mn_{1-x}Ti_xCoSb$ alloys.

When a Mn atom is introduced into the TiCoSb host lattice, as shown in Fig. 8, the Mn defect states create several bands directly at the Fermi level. These bands are essentially flat, indicative of very little interaction between the defect Mn d electrons and the orbitals of the host crystal. The Mn-rich superstructure, shown in Fig. 8, yields an entirely different response. The Ti defect states do not dramatically alter the overall electronic structure; instead the defect states exist primarily above the Fermi level with each band exhibiting greater curvature than the Mn defect states of the Ti-rich superstructure. When comparing the defect band structures shown in Fig. 8 with their end-members, it is therefore clear that the Ti-rich solvus line will be much steeper than the Mn-rich solvus line. A Ti-rich alloy of the form $Mn_{1-x}Ti_xCoSb$ will be driven to phase separate because the unhybridized Mn defect states that would otherwise exist can be removed by producing a mixture of the valence-precise TiCoSb and a metallic MnCoSb intermetallic with unambiguously hybridized Co-d–Mn-d states. When considering Mn-rich alloys, however, the introduction of a Ti defect does not dramatically disturb the underlying MnCoSb band structure. There is certainly still a driving force to phase separate at $T = 0$ K because of how energetically favorable it is to produce the valence-precise TiCoSb; however, the positive energy of formation is only 0.18 eV and can therefore be overcome by configurational entropy contributions that arise at elevated processing temperatures.

The energetics of the related alloy system $Zr_{1-x}Ti_xCoSb$, however, with a lattice misfit essentially three times the mag-

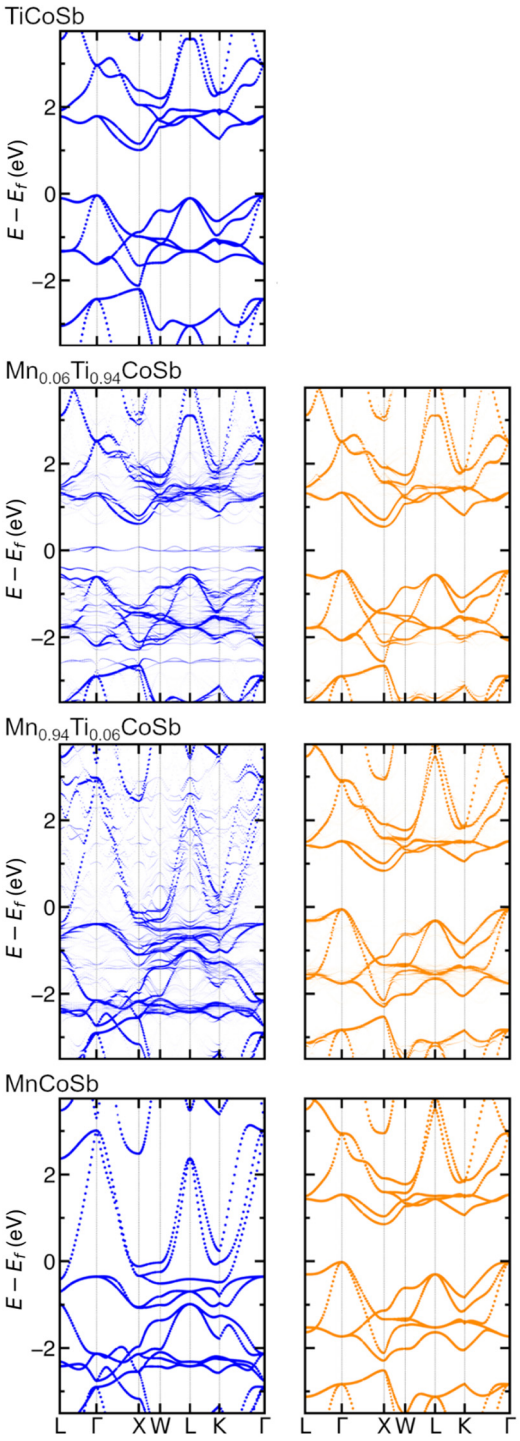

FIG. 8. Band structures of the candidate alloy system $Mn_{1-x}Ti_xCoSb$. The majority spin channel is shown in blue, and the minority spin channel is shown in orange. The band structure of TiCoSb reflects its semiconducting nature. An indirect band gap exists between the Γ and X points. The introduction of a Mn solute atom within $Mn_{0.06}Ti_{0.94}CoSb$ leads to the formation of defect electronic states that remain unhybridized with the host crystal, whereas the Ti solute atom within $Mn_{0.94}Ti_{0.06}CoSb$ only slightly disturbs the metallic majority spin channel. The band structure of MnCoSb displays half-metallic ferromagnetism.

nitude of $Mn_{1-x}Ti_xCoSb$, can be easily stabilized as a solid solution at elevated processing temperatures. We have found that the energy of formation for a Ti-rich alloy within this pseudobinary system is 0.15 eV while the energy formation for a Zr-rich alloy is 0.13 eV, both of which fall significantly below the 0.28 eV threshold. This result is consistent with previous studies that evaluated the phase space that consisted of the isovalent alloys of the form (Ti, Zr, Hf)NiSn [7]. The driving force for phase separation within the family of half-Heusler alloys is therefore clearly electronic in nature, and this fact should be acknowledged when considering whether a theoretically interesting candidate alloy can be realized experimentally.

B. Response of half-Heusler/Heusler systems to alloying

Arguably the most studied subset of candidate alloys within the family of Heuslers and half-Heuslers are the alloys with a general formula of $XY_{1+x}Z$, which will be referred to as half-Heusler/Heusler alloy candidates. These alloys can be thought of as the resulting structure when the Y-site element of the half-Heusler is used to populate the sublattice of vacancies that are fully occupied by the Y-site element in the Heusler structure. One of the most notable examples is $TiNi_{1+x}Sn$, which has been extensively studied both theoretically [6] and experimentally [26,27]. The appeal of these systems has often been linked to the large thermoelectric figure of merit, ZT, that is attributed to the presence of Heusler precipitates within a semiconducting half-Heusler matrix. Interestingly, all of the half-Heusler/Heusler systems that demonstrate a large thermoelectric figure of merit consist of a semiconducting half-Heusler phase with 18 valence electrons and a metallic Heusler phase with greater than 18 valence electrons. Our work clearly demonstrates that this fact is a direct consequence of the electronic disparity that exists between the semiconducting half-Heusler phase and the metallic Heusler. A majority of the half-Heusler/Heusler candidate alloys, summarized in Table VIII of the Appendix and plotted alongside the half-Heusler alloys in Fig. 7, possess energies of formation well above those of the end-members. The half-Heusler/Heusler systems $MgNi_{1+x}Sb$ and $MnNi_{1+x}Sb$, however, are expected to demonstrate significant interstitial solubility at reasonable processing temperatures.

$TiNi_{1+x}Sn$ serves as a prototypical immiscible half-Heusler/Heusler alloy system since, as mentioned previously, this material system has received considerable attention experimentally because the miscibility gap that exists between TiNiSn and $TiNi_2Sn$ yields microstructures that possess promising thermoelectric properties. Past theoretical studies, such as the work of Page *et al.*, performed cluster expansions on $MNi_{1+x}Sn$ (M = Ti, Zr, Hf) to demonstrate that the solid solubility of Ni interstitials within the half-Heuslers MNiSn is minimal [6]. Our work clearly shows that this minimal solubility is a direct consequence of the electronic stability of the half-Heusler TiNiSn. Similar to the alloying response of $Mn_{1-x}Ti_xCoSb$, the incorporation of a Ni interstitial within half-Heusler TiNiSn, as shown in Fig. 9, immediately disrupts the low-energy configuration of TiNiSb and produces a set of flat bands at the Fermi level. Although the lattice misfit is only $|\delta| = 2.86\%$, the highly unstable, unhybridized defect states caused by the Ni interstitial drive phase separation within this system as the energy of formation for $TiNi_{1.06}Sn$ is $\Delta E_f = 0.40$ eV. When introducing a vacancy onto one of the Ni sublattices of the Heusler, the energy penalty is still large enough to expect phase separation at any reasonable processing temperature ($\Delta E_f = 0.34$ eV); yet there is an asymmetry in the energetics of alloy candidates $TiNi_{1.06}Sn$ and $TiNi_{1.94}Sn$. In fact, when referring to the band structure of $TiNi_{1.94}Sn$ relative to pristine $TiNi_2Sn$, the band structure of $TiNi_{1.94}Sn$ remains fairly similar to that of $TiNi_2Sn$. The persistent driving force for phase separation within this system across all compositions must therefore be caused by the significant lowering in energy that can be achieved by decomposing into the semiconducting half-Heusler.

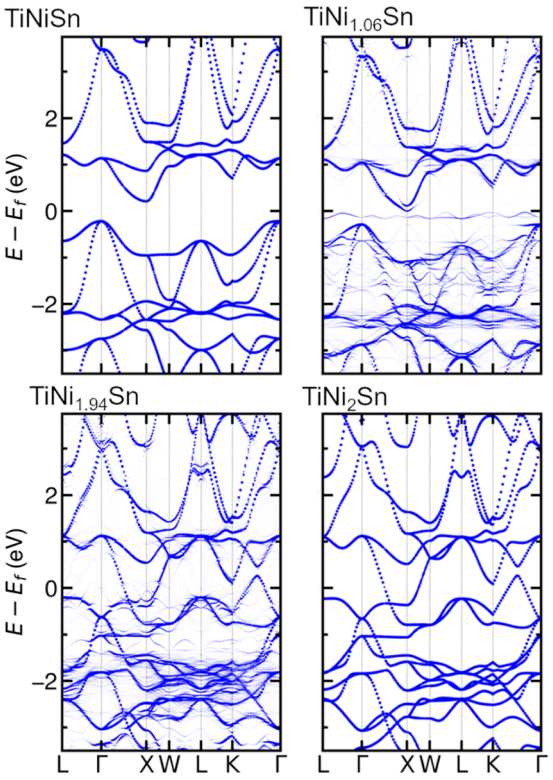

FIG. 9. Band structures of the candidate alloy system $TiNi_{1+x}Sn$. Only the spin majority channel is shown because the two channels are degenerate. The band structure of TiNiSn captures the semiconducting behavior of this 18-valence-electron half-Heusler. The Ni interstitial within $TiNi_{1.06}Sn$ leads to the formation of unhybridized electronic states that lie at the Fermi level, while the Ni vacancy within $TiNi_{1.94}Sn$ almost completely preserves the band structure of $TiNi_2Sn$. $TiNi_2Sn$ is a 28-valence-electron metallic Heusler that does not exhibit ferromagnetism.

The energetics of the $MgNi_{1+x}Sb$ system are noteworthy because the large negative energy of formation ($\Delta E_f = -0.19$) observed for the alloy candidate $MgNi_{1.06}Sb$ may very well be a direct consequence of the fact that MgNiSb is a 17-valence-electron half-Heusler. With this in mind, it does not necessarily come as a surprise that incorporating Ni interstitials may lead to a notably stable composition where semiconducting behavior is demonstrated. This has in fact been observed for the seemingly 17-valence-electron half-

Heusler TiFeSb, where Naghibolashrafi *et al.* discovered that when attempting to synthesize either TiFeSb or $TiFe_2Sb$, the predominate phase was of composition $TiFe_{1.5}Sb$ [40]. The stable crystal structure of $TiFe_{1.5}Sb$ was then posited to be a layering of $L2_1$ $TiFe_2Sb$ and $C1_b$ TiFeSb along the [111] direction of the underlying cubic lattice leading to a crystal structure with space group $R3m$. Remarkably, this $R3m$ phase was found to be a semiconductor. Although it is beyond the scope of our work to demonstrate the true ground state along the pseudobinary $MgNi_{1+x}Sb$, the dramatic decrease in energy that is accompanied by the incorporation of Ni interstitials certainly implies that MgNiSb does not truly belong on the convex hull of Mg-Ni-Sb. A great deal of insight into the true tunability of the Heusler and half-Heusler families can therefore be gained from the solute supercell calculations shared in this paper. As the materials community continues to push for effective computationally assisted solid state synthesis, and the discovery of material systems with outstanding electronic properties, it is absolutely essential to evaluate thermodynamic stability and assess the feasibility of obtaining alloys along the tie line between two ostensibly stable end-members.

Lastly, $MnNi_{1+x}Sb$, an alloy candidate between two metallic end-members, does not demonstrate either negative energies of formation or large positive energies of formation that would imply a driving force for phase separation. Instead, stabilizing $MnNi_{1.06}Sb$ and $MnNi_{1.94}Sb$ requires overcoming an energy of formation of $\Delta E_f = 0.13$ eV and $\Delta E_f = 0.11$ eV, respectively. These formation energies imply that a solid solution along the entire pseudobinary tie line should almost certainly exist above processing temperatures as low as 700 K, a fact that has been proven experimentally [41]. The positive energy of formation that is required to stabilize a Ni interstitial in MnNiSb can therefore be attributed predominantly to the lattice misfit that is present within this system—similar to the behavior of the previously discussed alloy system $Zr_{1-x}Ti_xCoSb$. Overall this finding reiterates the electronic-structure-dependent phase separation that exists within the family of half-Heuslers and Heuslers: Whereas semiconducting TiNiSn and metallic $TiNi_2Sn$ clearly phase separate across the entire tie line, $MnNi_{1+x}Sb$, which connects two metallic end-members, can be stabilized as a solid solution across the entire tie line at reasonable processing temperatures.

C. Response of Heusler systems to alloying

Naturally, one may expect electron-rich Heusler/Heusler alloys to possess a large driving force for phase separation analogous to that of the half-Heuslers; however, as shown in Fig. 7, this does not appear to be true. In particular, the candidate alloy system $Mn_{1-x}V_xFe_2Al$ appears to be completely miscible even though $MnFe_2Al$ has 26 valence electrons and VFe_2Al has 24 valence electrons. This speaks to the stark contrast in the nature of bonding within the half-Heuslers and Heuslers. As discussed previously, the band gap in semiconducting half-Heuslers is caused by the hybridization of the d orbitals of the transition metal elements at the X-site and Y-site, whereas the higher-symmetry Heusler alloys exhibit a much smaller gap due to weaker hybridization between the two unique Y sites of the Heusler structure. With this in mind, one can rationalize that alloying on the X site of a Heusler alloy, even in such a way as to disturb the semiconducting behavior of the host lattice, does not significantly destabilize the resulting solid solution because the states lying closest to the Fermi level are determined by Y-Y hybridization. Interestingly, this is further confirmed by the candidate alloy system $NbCo_{2x}Ru_{2-2x}Al$, which consists of 26-valence-electron $NbCo_2Al$ and 24-valence-electron $NbRu_2Al$, as both solid solutions for this system exceed the energy of formation threshold of 0.28 eV with energies of formation of 0.34 and 0.35 eV for the theoretical Co-rich and Ru-rich supercells, respectively. It does not appear to be coincidental that alloying on the Y site of a semiconducting Heusler alloy yields a much higher tendency for phase separation to occur. Tables V, VI, and VII in the Appendix report the energetics of all X-site, Y-site, and Z-site Heusler alloy candidates studied in this paper.

D. The impact of electron correlation on solubility

Interestingly, over the course of this study, a number of systems within the subset of Heusler-Heusler alloy candidates—specifically, alloy candidates that included a half-metallic Heusler and a metallic Heusler—were found to have energies of formation greater than 1 eV. At first it was believed that these systems demonstrated a tendency for half-metallic and metallic Heusler alloys to phase separate; however, these particular systems develop states with relatively narrow energy bands, and it is therefore pertinent to ask whether electron correlations of the Hubbard U type would aid or hinder phase separation. For this reason, a number of representative systems, summarized in Table I, were selected to investigate the impact of electron correlation on the energetics of alloy formation in the family of half-Heuslers and Heuslers.

Based on these additional calculations, it became clear that energies of formation greater than 1 eV are artifacts of the GGA calculations, and that an accurate representation of these alloy systems requires the consideration of electron correlation. Specifically, the inclusion of a U parameter for the systems with energies of formation greater than 1 eV led to a significant increase of charge localization on the solute atom and produced magnetic moments in line with the well-known Slater-Pauling behavior of half-Heusler and Heusler alloys. Alloy candidates that were found to phase separate and demonstrated magnetic moments in line with the Slater-Pauling rule before the inclusion of a U parameter, however, continued to show a propensity for phase separation after the inclusion of a U parameter. Therefore, even though the inclusion of a U parameter is purely qualitative in this paper (as described in Methods), we have found that the GGA functional provides accurate predictions with respect to the solubility of the candidate alloys considered here as long as the location of the defect states is qualitatively correct and ultimately yields the anticipated Slater-Pauling behavior. As discussed extensively in the literature, this behavior is in line with the fact that orbital-dependent potentials, such as that of the Hubbard-U-type electron correlation, will lift otherwise degenerate d orbitals of a $3d$ transition metal solute atom [42,43].

TABLE I. The energetics of incorporating a solute atom into a candidate alloy system as a function of U_{eff} values in GGA + U calculations based on the formalism outlined by Dudarev *et al.* [37] (see Methods). An accurate description of the alloying response of a candidate alloy system always corresponds to the set of calculations that accurately capture the well-known Slater-Pauling behavior of Heuslers and half-Heuslers. ΔE_f values are given in eV. Mag., magnetic moment in μ_B.

$Mn_{1-x}Ti_xNi_2Al$	ΔE_f^{Ti}	Mag.	ΔE_f^{Mn}	Mag.
U_{00}	0.14	4.02	1.19	0.13
U_{05}	0.17	4.39	0.12	3.61
U_{10}	0.21	4.59	0.09	3.75
$V_{1-x}Fe_xCo_2Ga$	ΔE_f^{Fe}	Mag.	ΔE_f^{V}	Mag.
U_{00}	0.16	2.19	0.18	4.82
U_{05}	0.18	2.19	0.13	4.86
U_{10}	0.14	2.19	0.02	4.96
$Mn_{1-x}Nb_xCo_2Al$	ΔE_f^{Nb}	Mag.	ΔE_f^{Mn}	Mag.
U_{00}	−0.12	3.88	0.12	2.12
U_{05}	−0.27	3.96	0.05	2.12
U_{10}	−0.37	4.46	0.02	2.13
$Nb_{1-x}Fe_xCo_2Al$	ΔE_f^{Fe}	Mag.	ΔE_f^{Nb}	Mag.
U_{00}	1.45	1.94	0.47	4.80
U_{05}	2.00	1.94	0.44	4.81
U_{10}	0.57	2.19	0.42	4.81
$Mn_{1-x}Ti_xCoSb$	ΔE_f^{Ti}	Mag.	ΔE_f^{Mn}	Mag.
U_{00}	0.19	3.00	0.55	3.00
U_{05}	0.13	3.17	0.51	3.00
U_{10}	−0.62	4.37	0.34	3.00

V. CONCLUSIONS

We have established the main driving force for phase separation within a host half-Heusler, Heusler, or half-Heusler/Heusler candidate alloy to be the electronic contribution of the solute atom. For half-Heuslers and half-Heusler/Heusler alloy candidates it is clear that the dramatic decrease in energy accompanied by the decomposition into a valence-precise ordered half-Heusler intermetallic will lead to a large miscibility gap along the tie line. While this lowering in energy can almost never be overcome in electron-rich half-Heusler/Heusler candidate alloys because of the additional energy penalty that is associated with the large lattice misfit between the end-members, there can exist electron-rich half-Heusler alloys where large amounts of the element that is unique to the semiconducting end-member can be miscible within the metallic end-member. Lattice misfit therefore plays a secondary role when considering the substitutional alloying behavior of half-Heusler and half-Heusler/Heusler alloys. When a lattice misfit on the order of 4–5% exists between end-members, high processing temperatures will be needed to stabilize a solid solution (processing temperatures on the order of 800 or 900 °C), but a solid solution should still be accessible over the entire tie line. When considering the potential for alloying to occur between two Heusler end-members, electron count is no longer a clear classifier.

In general it is not expected that a valence-precise Heusler end-member with 24 valence electrons will yield a phase-separated mixture along the tie line. This can be understood based on the fact that the band gap in a Heusler is caused by d-orbital hybridization between the two unique Y atoms of a Heusler compound with general formula XY_2Z. This band gap is quite small, especially in relation to the half-Heusler band gap caused by d-orbital hybridization between the X and Y elements. The crystal structure of a valence-precise Heusler is therefore more likely to accommodate the electronic states introduced by a solute atom.

Since some of the systems considered here develop states with relatively narrow energy bands, electron correlations of the Hubbard U type can significantly impact the energetics of alloy formation. Specifically, GGA calculations performed on several candidate Heusler/Heusler alloys do not properly predict the localized defect states of the solute atom and ultimately yield inaccurate magnetic moments without the inclusion of an orbital-dependent U parameter.

Through rationalizing the thermodynamic stability of half-Heuslers and Heuslers that have been alloyed with one another, we have, on the basis of lattice misfit and electronic perturbations caused by solute atoms, identified the electronic structure of the end-members of the candidate alloy system of interest as a simple proxy for determining whether the candidate alloy system will phase separate or form a solid solution at elevated processing temperatures. This process is quite general and can therefore be applied to other material families as a metric to aid in the realization of stable alloys with interesting properties.

ACKNOWLEDGMENTS

We thank Bailey Rhodes for thoughtful discussions during the writing process. This work was supported by the Materials Research Science and Engineering Center (MRSEC) program of the National Science Foundation (NSF) through Grant No. DMR-1720256 (IRG-1) and employed the shared facilities of the MRSEC at UC Santa Barbara, a member of the Materials Research Facilities Network [44]. We acknowledge the use of computing facilities from the Center for Scientific Computing (NSF Grants No. DMR1720256 and No. CNS-1725797). J.A.M. is supported by the NSF Graduate Research Fellowship Program under Grant No. NSF DGE-2139319.

APPENDIX

In this Appendix, the energy of formation ΔE_f and lattice misfit $|\delta|$ are reported for all half-Heusler X-, Y-, and Z-site substitutions studied (Tables II, III, and IV, respectively), for all Heusler X-, Y-, and Z-site substitutions studied (Tables V, VI, and VII, respectively), and for all half-Heusler/Heusler substitutions studied (Table VIII).

TABLE II. Energy of formation ΔE_f and lattice misfit $|\delta|$ for all half-Heusler X-site substitutions studied. Each alloy is expressed in the form of Eq. (2): $X(A)YZ$, where A is the atom acting as the solute.

Alloy 1	ΔE_f (eV)	Alloy 2	ΔE_f (eV)	$\|\delta\|$ (%)
Mg(Sc)AuSn	0.27	Sc(Mg)AuSn	0.20	0.05
Mg(Sc)NiBi	0.18	Sc(Mg)NiBi	0.07	0.21
Mg(Sc)PdSb	0.16	Sc(Mg)PdSb	0.02	0.46
Zr(Hf)CoSb	0.00	Hf(Zr)CoSb	0.00	0.51
Zr(Hf)PdSn	0.00	Hf(Zr)PdSn	0.00	0.52
Mg(Sc)NiSb	0.18	Sc(Mg)NiSb	0.12	0.53
Zr(Hf)NiSn	0.00	Hf(Zr)NiSn	0.00	0.59
Mg(Sc)PtSb	0.14	Sc(Mg)PtSb	0.05	0.65
Sc(Hf)PtSn	0.05	Hf(Sc)PtSn	−0.04	0.68
Ti(Mn)CoSb	0.56	Mn(Ti)CoSb	0.18	1.22
Ti(Hf)PtSn	0.07	Hf(Ti)PtSn	0.06	2.39
Ti(Hf)NiSn	0.09	Hf(Ti)NiSn	0.08	2.77
V(Nb)FeSb	0.11	Nb(V)FeSb	0.10	2.82
Ti(Hf)CoSb	0.09	Hf(Ti)CoSb	0.08	2.94
Sc(Ti)PtSn	0.12	Ti(Sc)PtSn	0.08	3.00
Ti(Zr)NiSn	0.14	Zr(Ti)NiSn	0.13	3.27
Mg(Y)NiBi	0.39	Y(Mg)NiBi	0.30	3.34
Sc(Y)PtSb	0.11	Y(Sc)PtSb	0.08	3.40
Ti(Zr)CoSb	0.15	Zr(Ti)CoSb	0.13	3.47
Sc(Y)NiBi	0.16	Y(Sc)NiBi	0.10	3.55
Sc(Mn)NiSb	0.54	Mn(Sc)NiSb	0.48	3.60
Sc(Y)NiSb	0.14	Y(Sc)NiSb	0.17	3.78
Mg(Y)PtSb	0.37	Y(Mg)PtSb	0.25	4.02
Hf(Mn)CoSb	0.66	Mn(Hf)CoSb	0.43	4.04
Sc(Mn)PtSb	0.30	Mn(Sc)PtSb	0.34	4.36
Mg(Y)NiSb	0.47	Y(Mg)NiSb	0.38	4.48
Zr(Mn)CoSb	0.77	Mn(Zr)CoSb	0.53	4.53

TABLE III. Energy of formation ΔE_f and lattice misfit $|\delta|$ for all half-Heusler Y-site substitutions studied. Each alloy is expressed in a form similar to that of Eq. (2): $XY(A)Z$, where A is the atom acting as the solute.

Alloy 1	ΔE_f (eV)	Alloy 2	ΔE_f (eV)	$\|\delta\|$ (%)
MgPd(Pt)Sb	0.02	MgPt(Pd)Sb	0.02	0.00
ScPd(Pt)Sb	0.02	ScPt(Pd)Sb	0.01	0.18
HfPd(Pt)Sn	0.01	HfPt(Pd)Sn	0.01	0.31
ScPt(Au)Sn	−0.05	ScAu(Pt)Sn	−0.28	1.42
MgPd(Cu)Sb	−0.11	MgCu(Pd)Sb	−0.28	1.53
MgPt(Cu)Sb	−0.07	MgCu(Pt)Sb	−0.22	1.53
MgNi(Cu)Sb	−0.09	MgCu(Ni)Sb	−0.22	2.68
YNi(Pd)Bi	0.10	Y(Pd)NiBi	0.06	3.48
HfCo(Rh)Sb	0.14	HfRh(Co)Sb	0.11	3.67
NbFe(Ru)Sb	0.17	NbRu(Fe)Sb	0.14	3.75
HfNi(Pd)Sn	0.13	HfPd(Ni)Sn	0.10	3.83
YNi(Pt)Sb	0.15	YPt(Ni)Sb	0.11	3.84
ZrNi(Pd)Sn	0.13	ZrPd(Ni)Sn	0.10	3.90
HfNi(Pt)Sn	0.18	HfPt(Ni)Sn	0.14	4.13
MgAu(Cu)Sn	0.03	MgCu(Au)Sn	0.04	4.19
ScNi(Pt)Sb	0.15	ScPt(Ni)Sb	0.13	4.21
MgNi(Pd)Sb	0.02	MgPd(Ni)Sb	0.01	4.28
MgNi(Pt)Sb	0.06	MgPt(Ni)Sb	0.07	4.28
TiNi(Pt)Sn	0.17	TiPt(Ni)Sn	0.13	4.69

TABLE IV. Energy of formation ΔE_f and lattice misfit $|\delta|$ for all half-Heusler Z-site substitutions studied. Each alloy is expressed in a form similar to that of Eq. (2): $XYZ(A)$, where A is the atom acting as the solute.

Alloy 1	ΔE_f (eV)	Alloy 2	ΔE_f (eV)	$\|\delta\|$ (%)
MgCuSn(Sb)	0.00	MgCuSb(Sn)	−0.11	0.09
ScPtSn(Sb)	−0.03	ScPtSb(Sn)	−0.23	0.46
YNiSb(Bi)	0.02	YNiBi(Sb)	0.04	2.01
ZrCoSb(Bi)	0.02	ZrCoBi(Sb)	0.01	2.09
ScNiSb(Bi)	0.02	ScNiBi(Sb)	0.02	2.26
MgNiSb(Bi)	0.04	MgNiBi(Sb)	0.05	3.06

TABLE V. Energy of formation ΔE_f and lattice misfit $|\delta|$ for all Heusler X-site substitutions studied. Each alloy is expressed in the form of Eq. (2): $X(A)Y_2Z$, where A is the atom acting as the solute.

Alloy 1	ΔE_f (eV)	Alloy 2	ΔE_f (eV)	$\|\delta\|$ (%)
Fe(Mn)Co_2Al	−0.11	Mn(Fe)Co_2Al	−0.04	0.04
Hf(Sc)Cu_2Al	−0.21	Sc(Hf)Cu_2Al	−0.18	0.10
Mn(V)Fe_2Al	−0.01	V(Mn)Fe_2Al	−0.11	0.52
Hf(Sc)Pd_2Al	−0.05	Sc(Hf)Pd_2Al	−0.06	0.54
Sc(Zr)Cu_2Al	−0.16	Zr(Sc)Cu_2Al	−0.18	0.57
Hf(Zr)Cu_2Al	0.00	Zr(Hf)Cu_2Al	0.00	0.67
Fe(V)Co_2Ga	0.18	V(Fe)Co_2Ga	0.16	0.98
Nb(Zr)Co_2Al	−0.05	Zr(Nb)Co_2Al	−0.06	1.80
Ti(V)Fe_2Ga	−0.05	V(Ti)Fe_2Ga	−0.29	1.94
Fe(Ti)Co_2Ga	0.20	Ti(Fe)Co_2Ga	0.20	1.96
Ti(V)Fe_2Al	−0.02	V(Ti)Fe_2Al	−0.17	2.17
Nb(Ti)Co_2Al	0.05	Ti(Nb)Co_2Al	0.04	2.20
Mn(Ti)Co_2Al	−0.05	Ti(Mn)Co_2Al	−0.01	2.29
Mn(Ti)Fe_2Al	0.14	Ti(Mn)Fe_2Al	0.26	2.64
Hf(Ti)Cu_2Al	0.04	Ti(Hf)Cu_2Al	0.07	2.86
Sc(Ti)Cu_2Al	−0.14	Ti(Sc)Cu_2Al	−0.10	2.96
Ti(Zr)Cu_2Al	0.11	Zr(Ti)Cu_2Al	0.05	3.43
Ti(Zr)Co_2Al	0.14	Zr(Ti)Co_2Al	0.19	4.08
Mn(Nb)Co_2Al	−0.12	Nb(Mn)Co_2Al	0.12	4.40
Mn(Zr)Co_2Al	0.39	Zr(Mn)Co_2Al	0.30	6.12

TABLE VI. Energy of formation ΔE_f and lattice misfit $|\delta|$ for all Heusler Y-site substitutions studied. Each alloy is expressed in the form of Eq. (2): $XY(A)Z$, where A is the atom acting as the solute and the Y atom populates all remaining lattice sites of the two distinct Y sublattices.

Alloy 1	ΔE_f (eV)	Alloy 2	ΔE_f (eV)	$\|\delta\|$ (%)
TiFe(Co)Al	−0.16	TiCo(Fe)Al	−0.13	0.06
TiFe(Co)Ga	−0.14	TiCo(Fe)Ga	−0.08	0.07
ScAg(Au)Al	−0.10	ScAu(Ag)Al	−0.17	0.20
MnCo(Fe)Al	0.09	MnFe(Co)Al	0.09	0.41
TiFe(Ni)Ga	−0.23	TiNi(Fe)Ga	−0.08	1.13
TiFe(Ni)Al	−0.29	TiNi(Fe)Al	−0.10	1.24
MnCo(Ni)Al	−0.10	MnNi(Co)Al	0.04	1.66
MnFe(Ni)Al	0.25	MnNi(Fe)Al	0.05	2.06
TiCu(Ni)Al	−0.11	TiNi(Cu)Al	0.01	2.38
ScPd(Cu)In	0.03	ScCu(Pd)In	0.10	2.40
ScCu(Pd)Al	0.13	ScCu(Pd)Al	0.03	2.69
ZrCo(Cu)Al	0.25	ZrCu(Co)Al	−0.03	2.98
ScCu(Pd)Ga	0.14	ScCu(Pd)Ga	0.05	2.99
ScAu(Pd)Al	0.01	ScPd(Au)Al	0.01	3.24
HfCu(Pd)Al	−0.09	HfPd(Cu)Al	0.04	3.31
ScAg(Pd)Al	0.01	ScPd(Ag)Al	0.06	3.44
TiCu(Co)Al	0.00	TiCo(Cu)Al	0.20	3.60
TiCu(Fe)Al	−0.02	TiFe(Cu)Al	−0.08	3.66
NbCo(Ru)Al	0.34	NbRu(Co)Al	0.35	3.66
MnNi(Rh)Al	0.16	MnRh(Ni)Al	−0.07	4.00
MnCo(Rh)Al	0.19	MnRh(Co)Al	0.16	5.61
MnFe(Rh)Al	0.30	MnRh(Fe)Al	0.27	5.99
ScAu(Cu)Al	0.00	ScCu(Au)Al	0.07	6.10
ScAg(Cu)Al	0.13	ScCu(Ag)Al	0.18	6.31

TABLE VII. Energy of formation ΔE_f and lattice misfit $|\delta|$ for all Heusler Z-site substitutions studied. Each alloy is expressed in the form of Eq. (2): $XY_2Z(A)$, where A is the atom acting as the solute.

Alloy 1	ΔE_f	Alloy 2	ΔE_f	$\|\delta\|$
$TiFe_2Al(Ga)$	−0.01	$TiFe_2Ga(Al)$	−0.01	0.06
$ScPd_2Sn(In)$	−0.03	$ScPd_2In(Sn)$	−0.02	0.07
$ScPd_2Al(Ga)$	−0.02	$ScPd_2Ga(Al)$	−0.03	0.08
$ScCu_2Al(Ga)$	0.00	$ScCu_2Ga(Al)$	−0.01	0.22
$MnCo_2Al(Ga)$	−0.00	$MnCo_2Ga(Al)$	0.00	0.37
$MnCo_2Al(Ge)$	−0.16	$MnCo_2Ge(Al)$	−0.15	0.65
$MnRh_2Al(Ge)$	−0.36	$MnRh_2Ge(Al)$	−0.34	0.73
$MnCo_2Al(Si)$	−0.20	$MnCo_2Si(Al)$	0.17	1.23
$ScPd_2Al(In)$	0.01	$ScPd_2In(Al)$	−0.06	3.02
$ScPd_2In(Ga)$	0.04	$ScPd_2Ga(In)$	0.07	3.02
$ScPd_2Al(Sn)$	0.00	$ScPd_2Sn(Al)$	−0.13	3.09
$MgAg_2Zn(Cd)$	0.04	$MgAg_2Cd(Zn)$	−0.02	3.14
$ScCu_2Al(In)$	0.03	$ScCu_2In(Al)$	−0.06	3.31
$TiFe_2Ga(Sn)$	0.16	$TiFe_2Sn(Ga)$	−0.09	3.45
$TiFe_2Al(Sn)$	0.10	$TiFe_2Sn(Al)$	−0.19	3.51
$ScCu_2Ga(In)$	0.11	$ScCu_2In(Ga)$	0.09	3.52
$MnCo_2Al(Sn)$	0.23	$MnCo_2Sn(Al)$	0.16	4.89
$MnCo_2Al(Sb)$	−0.11	$MnCo_2Sb(Al)$	−0.28	5.35

TABLE VIII. Energy of formation ΔE_f and lattice misfit $|\delta|$ for all half-Heusler/Heusler substitutions studied in this paper. Each alloy is expressed in the form of $XY_{1+x}Z$, where x describes the extent to which the second Y sublattice of the Heusler XY_2Z is occupied.

Alloy 1	ΔE_f (eV)	Alloy 2	ΔE_f	$\|\delta\|$ (%)
$MgNi_{1.06}Sb$	−0.19	$MgNi_{1.94}Sb$	−0.01	1.55
$MnNi_{1.06}Sb$	0.13	$MnNi_{1.94}Sb$	0.11	2.58
$ZrNi_{1.06}Sn$	0.48	$ZrNi_{1.94}Sn$	0.34	2.60
$HfNi_{1.06}Sn$	0.54	$HfNi_{1.94}Sn$	0.40	2.63
$TiNi_{1.06}Sn$	0.40	$TiNi_{1.94}Sn$	0.34	2.86
$YPd_{1.06}Bi$	0.44	$YPd_{1.94}Bi$	0.30	2.96
$NbCo_{1.06}Sn$	0.60	$NbCo_{1.94}Sn$	0.60	3.04

[1] F. Heusler, W. Starck, and E. Haupt, Magnetisch-chemische studien, Verh. Deut. Phys. Ges. **5**, 219 (1903).

[2] L. Néel, Propriétés magnétiques de l'état métallique et énergie d'interaction entre atomes magnétiques, Ann. Phys. (Paris) **11**, 232 (1936).

[3] T. Graf, C. Felser, and S. S. P. Parkin, Simple rules for the understanding of Heusler compounds, Prog. Solid State Chem. **39**, 1 (2011).

[4] S. Chadov, X. Qi, J. Kübler, G. H. Fecher, C. Felser, and S. C. Zhang, Tunable multifunctional topological insulators in ternary Heusler compounds, Nat. Mater. **9**, 541 (2010).

[5] Z. Wang, M. G. Vergniory, S. Kushwaha, M. Hirschberger, E. V. Chulkov, A. Ernst, N. P. Ong, R. J. Cava, and B. A. Bernevig, Time-Reversal-Breaking Weyl Fermions in Magnetic Heusler Alloys, Phys. Rev. Lett. **117**, 236401 (2016).

[6] A. Page, C. Uher, P. F. Poudeu, and A. Van der Ven, Phase separation of full-Heusler nanostructures in half-Heusler thermoelectrics and vibrational properties from first-principles calculations, Phys. Rev. B **92**, 174102 (2015).

[7] A. Page, A. Van der Ven, P. F. P. Poudeu, and C. Uher, Origins of phase separation in thermoelectric (Ti, Zr, Hf)NiSn half-Heusler alloys from first principles, J. Mater. Chem. A **4**, 13949 (2016).

[8] V. Kocevski and C. Wolverton, Designing high-efficiency nanostructured two-phase Heusler thermoelectrics, Chem. Mater. **29**, 9386 (2017).

[9] J. M. Mena, H. G. Schoberth, T. Gruhn, and H. Emmerich, Nanophase separation in CoSb-based half-Heusler thermoelectrics: A multiscale simulation study, Phys. Status Solidi A **213**, 706 (2016).

[10] R. A. de Groot, F. M. Mueller, P. G. van Engen, and K. H. J. Buschow, New Class of Materials: Half-Metallic Ferromagnets, Phys. Rev. Lett. **50**, 2024 (1983).

[11] F. G. Aliev, N. B. Brandt, V. V. Kozyr'Kov, V. V. Moshchalkov, R. V. Skolozdra, Yu. V. Stadnyk, and V. K. Pecharskii,

Metal–insulator transition of *R*NiSn (R = Zr, Hf, Ti) intermetallic vacancy systems, JETP Lett. **45**, 684 (1987).
[12] S. Öğüt and K. M. Rabe, Band gap and stability in the ternary intermetallic compounds NiSnM (M = Ti, Zr, Hf): A first-principles study, Phys. Rev. B **51**, 10443 (1995).
[13] B. R. K. Nanda and I. Dasgupta, Electronic structure and magnetism in half-Heusler compounds, J. Phys.: Condens. Matter **15**, 7307 (2003).
[14] I. Galanakis, P. H. Dederichs, and N. Papanikolaou, Origin and properties of the gap in the half-ferromagnetic Heusler alloys, Phys. Rev. B **66**, 134428 (2002).
[15] H. C. Kandpal, C. Felser, and R. Seshadri, Covalent bonding and the nature of band gaps in some half-Heusler compounds, J. Phys. D: Appl. Phys. **39**, 776 (2006).
[16] Y. Nishino, C. Kumada, and S. Asano, Phase stability of Fe_3Al with addition of 3d transition elements, Scr. Mater. **36**, 461 (1997).
[17] S. Ishida, S. Fujii, S. Kashiwagi, and S. Asano, Search for half-metallic compounds in Co_2MnZ (Z = IIIb, IVb, Vb element), J. Phys. Soc. Jpn. **64**, 2152 (1995).
[18] P. J. Brown, K. U. Neumann, P. J. Webster, and K. R. A. Ziebeck, The magnetization distributions in some Heusler alloys proposed as half-metallic ferromagnets, J. Phys.: Condens. Matter **12**, 1827 (2000).
[19] I. Galanakis, P. H. Dederichs, and N. Papanikolaou, Slater-Pauling behavior and origin of the half-metallicity of the full-Heusler alloys, Phys. Rev. B **66**, 174429 (2002).
[20] W. Hume-Rothery and G. V. Raynor, *The Structure of Metals and Alloys* (Institute of Metals, London, 1954).
[21] G. T. de Laissardiere, D. N. Manh, L. Magaud, J. P. Julien, F. Cyrot-Lackmann, and D. Mayou, Electronic structure and hybridization effects in Hume-Rothery alloys containing transition elements, Phys. Rev. B **52**, 7920 (1995).
[22] J. E. Saal, S. Kirklin, M. Aykol, B. Meredig, and C. Wolverton, Materials design and discovery with high-throughput density functional theory: the Open Quantum Materials Database (OQMD), JOM **65**, 1501 (2013).
[23] S. Kirklin, J. E. Saal, B. Meredig, A. Thompson, J. W. Doak, M. Aykol, S. Rühl, and C. Wolverton, The Open Quantum Materials Database (OQMD): assessing the accuracy of DFT formation energies, npj Comput. Mater. **1**, 15010 (2015).
[24] M. Liu, qmpy_rester, available at https://github.com/mohanliu/qmpy_rester.
[25] T. Graf, P. Klaer, J. Barth, B. Balke, H.-J. Elmers, and C. Felser, Phase separation in the quaternary Heusler compound $CoTi_{(1-x)}Mn_xSb$–A reduction in the thermal conductivity for thermoelectric applications, Scr. Mater. **63**, 1216 (2010).
[26] N. Verma, J. E. Douglas, S. Krämer, T. M. Pollock, R. Seshadri, and C. G. Levi, Microstructure evolution of biphasic $TiNi_{1+x}Sn$ thermoelectric materials, Metall. Mater. Trans. A **47**, 4116 (2016).
[27] J. E. Douglas, C. S. Birkel, M. Miao, C. J. Torbet, G. D. Stucky, T. M. Pollock, and R. Seshadri, Enhanced thermoelectric properties of bulk TiNiSn via formation of a $TiNi_2Sn$ second phase, Appl. Phys. Lett. **101**, 183902 (2012).
[28] M. L. C. Buffon, G. Laurita, N. Verma, L. Lamontagne, L. Ghadbeigi, D. L. Lloyd, T. D. Sparks, T. M. Pollock, and R. Seshadri, Enhancement of thermoelectric properties in the Nb–Co–Sn half-Heusler/Heusler system through spontaneous inclusion of a coherent second phase, J. Appl. Phys. (Melville, NY) **120**, 075104 (2016).
[29] Y. M. Eggeler, E. E. Levin, F. Wang, D. A. Kitchaev, A. Van der Ven, R. Seshadri, T. M. Pollock, and D. S. Gianola, Interfacial structure and strain accommodation in two-phase $NbCo_{1.2}Sn$ Heusler intermetallics, Phys. Rev. Materials **4**, 093601 (2020).
[30] G. Kresse and J. Furthmüller, Efficient iterative schemes for *ab-initio* total-energy calculations using a plane-wave basis set, Phys. Rev. B **54**, 11169 (1996).
[31] P. E. Blöchl, Projector augmented-wave method, Phys. Rev. B **50**, 17953 (1994).
[32] G. Kresse and D. Joubert, From ultrasoft pseudopotentials to the projector augmented-wave method, Phys. Rev. B **59**, 1758 (1999).
[33] J. P. Perdew, K. Burke, and M. Ernzerhof, Generalized Gradient Approximation Made Simple, Phys. Rev. Lett. **77**, 3865 (1996).
[34] H. J. Monkhorst and J. D. Pack, Special points for Brillouin-zone integrations, Phys. Rev. B **13**, 5188 (1976).
[35] V. Popescu and A. Zunger, Extracting E versus k effective band structure from supercell calculations on alloys and impurities, Phys. Rev. B **85**, 085201 (2012).
[36] Q. Zheng, VaspBandUnfolding, available at https://github.com/QijingZheng/VaspBandUnfolding.
[37] S. L. Dudarev, G. A. Botton, S. Y. Savrasov, C. J. Humphreys, and A. P. Sutton, Electron-energy-loss spectra and the structural stability of nickel oxide: An LSDA $+U$ study, Phys. Rev. B **57**, 1505 (1998).
[38] H. C. Kandpal, G. H. Fecher, C. Felser, and G. Schönhense, Correlation in the transition-metal-based Heusler compounds Co_2MnSi and Co_2FeSi, Phys. Rev. B **73**, 094422 (2006).
[39] S. Anand, K. Xia, V. I. Hegde, U. Aydemir, V. Kocevski, T. Zhu, C. Wolverton, and G. J. Snyder, A valence balanced rule for discovery of 18-electron half-Heuslers with defects, Energy Environ. Sci. **11**, 1480 (2018).
[40] N. Naghibolashrafi, S. Keshavarz, V. I. Hegde, A. Gupta, W. H. Butler, J. Romero, K. Munira, P. LeClair, D. Mazumdar, J. Ma, A. W. Ghosh, and C. Wolverton, Synthesis and characterization of Fe-Ti-Sb intermetallic compounds: Discovery of a new Slater-Pauling phase, Phys. Rev. B **93**, 104424 (2016).
[41] E. E. Levin, J. D. Bocarsly, K. E. Wyckoff, T. M. Pollock, and R. Seshadri, Tuning the magnetocaloric response in half-Heusler/Heusler $MnNi_{1+x}Sb$ solid solutions, Phys. Rev. Materials **1**, 075003 (2017).
[42] V. I. Anisimov, F. Aryasetiawan, and A. I. Lichtenstein, First-principles calculations of the electronic structure and spectra of strongly correlated systems: the LDA $+U$ method, J. Phys.: Condens. Matter **9**, 767 (1997).
[43] M. A. Korotin, A. V. Postnikov, T. Neumann, G. Borstel, V. I. Anisimov, and M. Methfessel, Electronic structure and lattice relaxation related to Fe in MgO, Phys. Rev. B **49**, 6548 (1994).
[44] https://www.mrfn.org.